PHYSICS

Floquet maser

Min Jiang[1,2,3], Haowen Su[1,2,3], Ze Wu[1,2,3], Xinhua Peng[1,2,3]*, Dmitry Budker[4,5,6]

The invention of the maser stimulated revolutionary technologies such as lasers and atomic clocks. Yet, realizations of masers are still limited; in particular, the physics of masers remains unexplored in periodically driven (Floquet) systems, which are generally defined by time-periodic Hamiltonians and enable observation of many exotic phenomena such as time crystals. Here, we investigate the Floquet system of periodically driven ^{129}Xe gas under damping feedback and unexpectedly observe a multimode maser that oscillates at frequencies of transitions between Floquet states. Our findings extend maser techniques to Floquet systems and open avenues to probe Floquet phenomena unaffected by decoherence, enabling a previously unexplored class of maser sensors. As a first application, our maser offers the capability of measuring low-frequency (1 to 100 mHz) magnetic fields with subpicotesla-level sensitivity, which is substantially better than state-of-the-art magnetometers and can be applied to, for example, ultralight dark matter searches.

INTRODUCTION

The masers (*1*–*4*) have become ubiquitous and resulted in innovations (*5*–*9*) ranging from lasers, atomic clocks, ultrasensitive magnetic resonance spectroscopy, and low-noise amplifiers to deep-space communications. Because the frequency of radiowaves produced by masers is highly stable, these devices enable exquisitely sensitive measurement of their frequency shifts caused by the interactions with external electromagnetic fields. This opens up exciting possibilities for developing precise metrology in applied and fundamental physics, such as magnetometry (*9*–*11*), temperature sensors (*12*), tests of Lorentz and charge-parity-time reversal symmetry violation (*13*), and searches for topological dark matter (*14*). The masers have been demonstrated in a variety of systems, such as ammonia molecules (*1*), hydrogen atoms (*6*), noble gas (*15*, *16*), pentacene molecules (*2*), and silicon- and nitrogen-vacancy defect materials (*3*, *4*, *10*). However, the demonstrations of masers have remained unexplored in periodically driven (Floquet) systems (*17*), limiting the broad applications in sensing, spectroscopy, and fundamental physics. The generalization of masers to periodically driven systems would pave the way for many new applications, such as ultralow-frequency magnetic field sensing (*18*, *19*) and searching for oscillating electric dipole moments (EDMs) [see review in (*20*, *21*)].

To reach the above goal, a proper periodically driven maser gain medium should be considered. The recently developed notion of Floquet system [see review in (*17*)], which is only invariant under discrete time translations by a period, has spawned intriguing prospects, such as time crystals (*22*) and Floquet topological insulators (*23*). A variety of Floquet systems have been realized through periodic driving, ranging from periodically driven trapped ions (*22*) and atomic ensembles (*23*, *24*) to nitrogen-vacancy centers (*25*). For the goal of developing periodically driven masers, Floquet systems should be an outstanding candidate. We note that the combination of maser techniques and Floquet systems can overcome the decoherence effect and thus permits a fresh look at many phenomena. For example, successful realization of maser using Floquet systems may open new opportunities for observing long-range temporal dynamics (*22*, *23*) and spectroscopy with submillihertz resolution, with important implications in quantum metrology (*26*–*28*), for example, in searches for gravitational waves in evolved Laser Interferometer Space Antenna (eLISA) with the bandwidth of 1 to 100 mHz (*18*), measurement of the worldwide magnetic-background noise (including attempts at earthquake prediction) (*19*), and axion dark matter searches (*29*–*31*). Despite these appealing features, a demonstration of masers based on Floquet systems was heretofore lacking.

Here, we report the first theoretical and experimental demonstration of a Floquet-based maser composed of periodically driven ^{129}Xe spins in a vapor cell. Unlike the common masers that exploit inherent transitions (*1*–*7*), our maser is based on the synthetic dimensions supported by Floquet states of the system. We name the observed maser "Floquet maser," which oscillates at the frequencies of transitions between Floquet states.

Using our maser technique, we observe ultrahigh-resolution spectra of the Floquet system with two orders of magnitude better resolution compared to that limited by decoherence. As the spectral resolution is greatly increased, a different regime emerges where high-order Floquet sidebands become notable and complex spectra are expected, enabling accurate measurement of physical parameters, e.g., atomic scalar and tensor polarizabilities (*28*), magnetic fields (*18*), ultralight bosonic exotic fields (*31*), and multiphoton coherences (*32*). As a first application, our maser constitutes a new quantum technology for measuring ultralow-frequency (1 to 100 mHz) magnetic fields with subpicotesla-level sensitivity, which is notably better than state-of-the-art magnetometers (*18*, *33*–*35*). Moreover, we show that the present maser technique allows us to achieve a search sensitivity for the coupling of axion dark matter to masing spins well beyond the most stringent existing constraints (*30*, *31*).

RESULTS

Setup and Floquet system

We use noble gas atoms ^{129}Xe with nuclear spin $I = 1/2$ in a setup depicted in Fig. 1A. A 0.5-cm^3 cubic vapor cell made from pyrex glass

[1]Hefei National Laboratory for Physical Sciences at the Microscale and Department of Modern Physics, University of Science and Technology of China, Hefei 230026, China. [2]CAS Key Laboratory of Microscale Magnetic Resonance, University of Science and Technology of China, Hefei 230026, China. [3]Synergetic Innovation Center of Quantum Information and Quantum Physics, University of Science and Technology of China, Hefei 230026, China. [4]Helmholtz-Institut, GSI Helmholtzzentrum für Schwerionenforschung, 55128 Mainz, Germany. [5]Johannes Gutenberg-Universität Mainz, 55128 Mainz, Germany. [6]Department of Physics, University of California, Berkeley, CA 94720-7300, USA.
*Corresponding author. Email: xhpeng@ustc.edu.cn

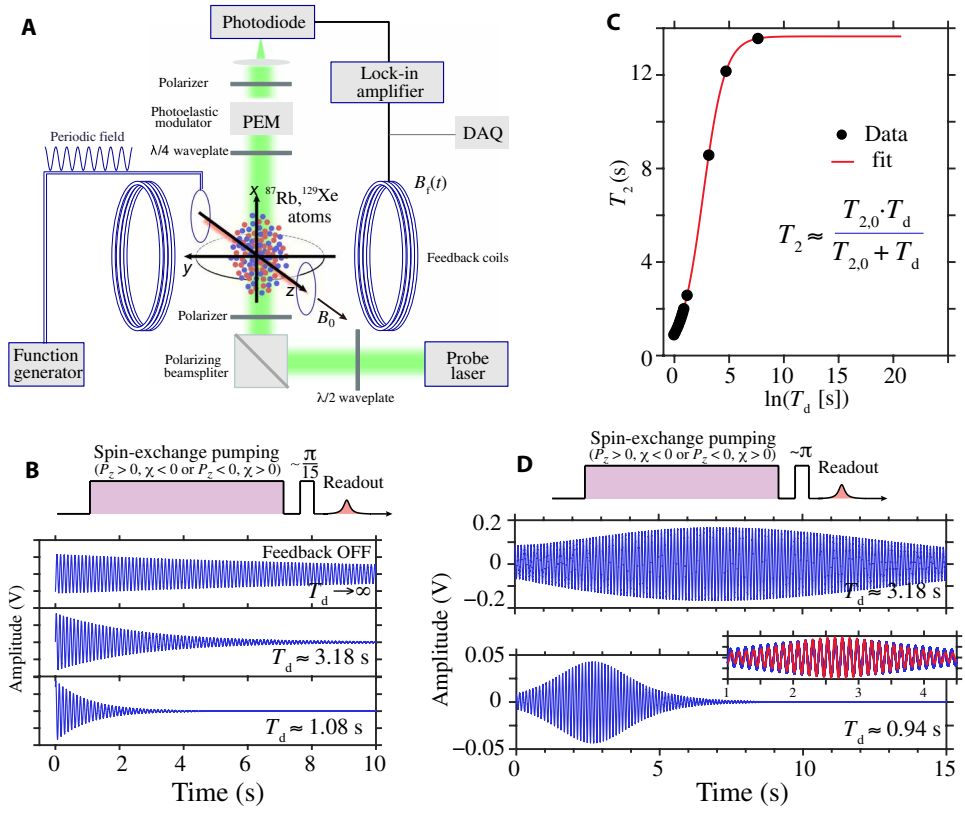

Fig. 1. Schematic of experimental setup and damping feedback mechanism. (**A**) Schematic of the Floquet ^{129}Xe nuclear-spin maser. The ^{129}Xe atoms are polarized and detected by spin-exchange collisions with optically pumped ^{87}Rb (see Materials and Methods). Under a bias field and an oscillating magnetic field along *z*, the ^{129}Xe spins are magnetically coupled to a feedback circuit, which feeds back real-time $B_f(t)$ along *y* and induces the damping of ^{129}Xe spins. DAQ, data acquisition. (**B**) Measured free decay ^{129}Xe signals for three different feedback gains (corresponding to different T_d). Here, the spin population P_z and the feedback gain χ are initially set as $P_z > 0$, $\chi<0$ or $P_z < 0$, $\chi>0$. T_d is well determined by corresponding decay time T_2 with $\sim \frac{\pi}{15}$ excitation angle (see the main text). (**C**) Measured decay time T_2 as a function of damping time (black symbols). The red line is a fit with $(T_{2,0}^{-1} + T_d^{-1})^{-1}$, where $T_{2,0}$ represents the intrinsic decoherence time without feedback. (**D**) Transient maser operations for two different damping times after flipping ~π angle, inducing the inversion of ^{129}Xe spins population. The decay signal can be fitted with a hyperbolic secant function shown in the inset (see Materials and Methods).

contains 5-torr ^{129}Xe, 250-torr N_2, and a droplet (several milligrams) of enriched ^{87}Rb. ^{129}Xe spins are polarized by spin-exchange collisions with optically pumped ^{87}Rb atoms in a bias magnetic field B_0 (≈750 nT) along the polarized direction (*z* axis) (*36*). Similar to a microwave cavity in conventional masers (*1*, *2*, *4*), the ^{129}Xe spins in our experiments are embedded in a feedback circuit (*16*) (see Fig. 1A), which uses an atomic magnetometer (*34*) as a sensitive detector of ^{129}Xe spins and simultaneously supplies the real-time output audio-frequency signal of the magnetometer to the spins (see Materials and Methods). The ^{87}Rb atoms in the vapor cell act as a magnetometer for measuring the ^{129}Xe spin polarization P_x along the *x* direction; a corresponding feedback field $B_f(t) = \chi P_x(t)$ is applied to the ^{129}Xe spins with a set of *y* coils around the vapor cell. Here, the proportionality constant χ (feedback gain) encapsulates the conversion factor of the atomic magnetometer and the connection polarity of the feedback coils. The amplitude of feedback gain χ can be adjusted with a rheostat in series with the feedback coils. The sign of χ can be controlled by the directions of the bias field (+*z* or −*z*) and feedback coils (+*y* or −*y*) (more details are presented in Materials and Methods). Similar to a resonant cavity (*37*), the self-induced feedback field $B_f(t)$ carries the information about the spins and then acts back on the spins, leading to the well-known phenomenon of damping (*9*, *38*) that is important in our maser scheme.

We consider a Floquet system, where an oscillating magnetic field $B_{ac} \cos(2\pi\nu_{ac}t)$ (along *z*) periodically drives Zeeman energy levels. Unfortunately, the textbook approach (*1*–*7*, *10*, *12*) used to analyze masers is not well-suited for periodically driven systems. As noted in the pioneering work (*39*), a system with a time-periodic Hamiltonian can be equivalently represented as a time-independent Hamiltonian but with an infinite number of static energy levels. Within this framework, we can borrow some essential notions from the conventional time-independent masers and this, in turn, leads to the entirely new concept of Floquet maser. Specifically, a Floquet system has eigenstates (Floquet states) $|\pm\rangle_n = \Sigma_{n'} \mathcal{J}_{n-n'}(\pm\gamma B_{ac}/2\nu_{ac})|\pm, n'\rangle$ (see Materials and Methods, Eq. 6) and energies $E_{\pm,n}/2\pi = \pm\nu_0/2 + n\nu_{ac}$ (*39*, *40*) (see Materials and Methods, Eq. 4). Here, $|\pm, n'\rangle$ denotes that the spin is in the spin-up ($|+\rangle$) state or in the spin-down ($|-\rangle$) state and the periodic driving field has the photon number n' (*39*, *40*). $\mathcal{J}_{n-n'}$ is the Bessel function of the first kind of order $n - n'$. Under periodic driving of the oscillating field, the two-level ($|+\rangle$, $|-\rangle$) spin system is extended to an infinite number of synthetic

energy levels $|\pm\rangle_n$ (see Fig. 2A), and these energy levels are time independent.

Masing effect on Floquet system

We first measure the feedback-induced damping of ^{129}Xe spins, because damping plays an important role in realizing masers (*9*, *16*, *38*). For simplicity, the periodic driving field is turned off when we measure damping. The measurement process is shown in Fig. 1B. The ^{129}Xe spins are initially polarized along $+z$ and the feedback gain is set as $\chi<0$, or the spins are initially polarized along $-z$ and the feedback gain is set as $\chi>0$. The spins are tilted by a small angle $\theta_0 \approx \frac{\pi}{15}$ with a magnetic field pulse along the x axis, and then the free decay of ^{129}Xe signals is measured under self-induced feedback. In this case, the free decay signal can be fitted with a single-exponential decay with a decay rate given by $T_{2,0}^{-1} + T_d^{-1}$ (see Materials and Methods), where the intrinsic decoherence time $T_{2,0} \approx 13.65(1)$ s and T_d (the damping time) depends on feedback gain χ. By fitting the experimental data, we can find the decay rate and then calculate the corresponding T_d under different feedback gains χ, as shown in Fig. 1B. The results show that, by coupling nuclear spins to the feedback circuit, a regime can be reached in which damping constitutes the dominant mechanism of spin relaxation, e.g., $T_d = 1.08(1)\text{s} \ll T_{2,0}$, and spin relaxation can be controlled by adjusting the feedback gain (Fig. 1C). This also suggests a method for active fast reset of long-lived spins [for example, ^{3}He noble gas (*41*)] to their equilibrium state, improving the repetition rate of an experiment.

We next measure the spin dynamics when the ^{129}Xe spin population is suddenly inverted, corresponding to the case of $\theta_0 \approx \pi$. Figure 1D gives the observed free decay signals with designed $T_d \approx 3.18$ s and 0.94 s, respectively. Unlike the exponential decay, the observed ^{129}Xe spin signal first increases to a maximum value at a certain time and then decays to zero, which can be described by a hyperbolic secant function (see Materials and Methods, Eq. 8). As first reported in (*38*), this is a transient maser when the threshold of the damping time $T_d/T_{2,0} \ll 1$ is fulfilled. However, the demonstrated maser cannot oscillate continuously because the population inversion is transient. To generate stationary maser dynamics (*1*, *4*, *12*), we can reverse the circular polarization of pump laser or alternatively reverse the sign of the feedback gain χ (see Materials and Methods) and simultaneously set the damping time smaller than the intrinsic decoherence time (i.e., $T_d/T_{2,0} < 1$). Under these conditions, coupling of the spins to the damping feedback circuit can produce a self-sustained masing signal (*9*, *16*).

We now consider the spin dynamics of the Floquet ^{129}Xe system under the damping feedback field. As discussed above, the Floquet system can be treated as a time-independent one with an infinite set of energy levels, shown in Fig. 2A. The key to a maser based on Floquet systems is the preparation of spin population between those Floquet states. In our experiments, population between Floquet states ($|+\rangle_n$ and $|-\rangle_m$) of the Floquet ^{129}Xe spins can be continuously prepared through ^{129}Xe–^{87}Rb spin-exchange collisions. Moreover, building on our demonstration of damping, the damping time is set to T_d

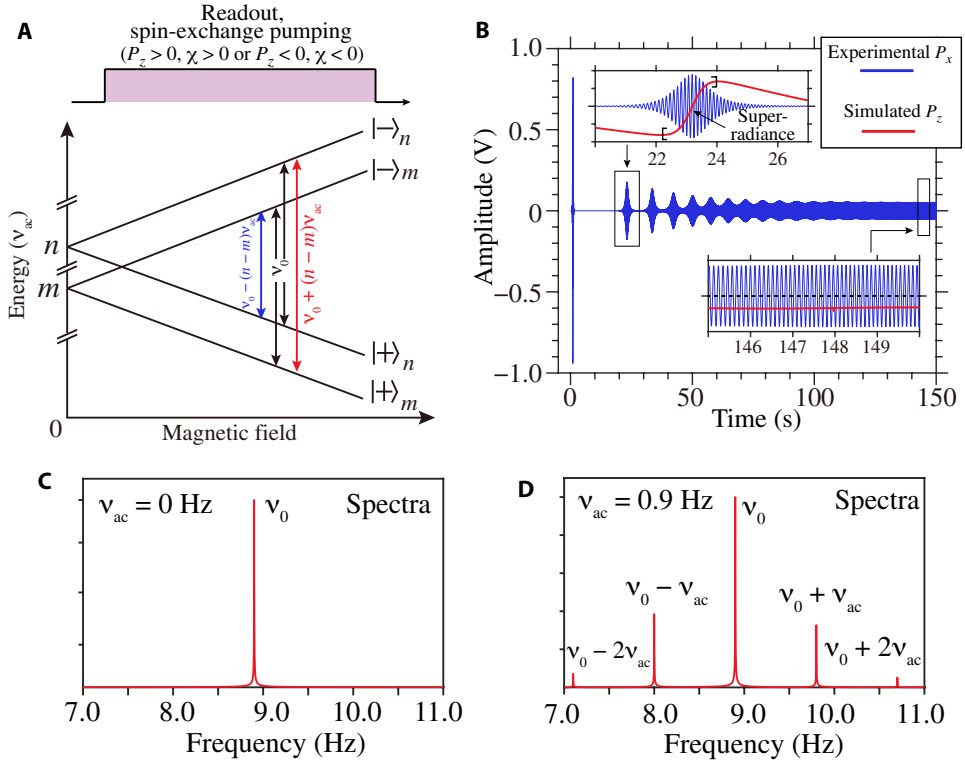

Fig. 2. Demonstration of Floquet maser. (**A**) Floquet states of a periodically driven two-level system (Floquet system). The energy gap between the upper and lower Floquet states $|+\rangle_n$ and $|-\rangle_m$ is $E_{n,m}/2\pi = (n-m)\nu_{ac} + \nu_0$. The spin population P_z and the feedback gain χ are set as $P_z > 0, \chi > 0$ or $P_z < 0, \chi < 0$. (**B**) Signal of ^{129}Xe Floquet maser. The insets are zoom-in plots for the signal and the simulated spin population (P_z). (**C** and **D**) The corresponding amplitude spectra of the maser signal after eliminating the transient [$\nu_{ac} = 0$ for (C); 0.9 Hz for (D)].

≈ 6.25 s, satisfying the threshold of $T_d/T_{2,0} < 1$. When the feedback circuit is suddenly on, a feedback $B_f(t)$ is induced by the Floquet system itself and oscillates with the frequencies of Floquet sidebands. The feedback field produces a torque on the spins that changes spin polarization (*9*, *16*). This self-coupling can lead to stimulated Rabi oscillations between the Floquet states $|+\rangle_n$ and $|-\rangle_m$. A steady-state maser oscillation is expected to build up. For different Floquet states pair n, m, the maser oscillation frequency is $E_{n,m}/2\pi = (n - m)\nu_{ac} + \nu_0$.

As a first illustration of the Floquet maser, Fig. 2B shows a time trace of ^{129}Xe spins under 0.900-Hz driving field and B_{ac} = 56.15 nT. The ^{129}Xe transverse polarization (P_x) shows characteristic initial transients, which subsequently level into a stationary oscillation. Because spin population (P_z) cannot be measured directly in our experiment, we simulate the maser with nonlinear Bloch equations (see Materials and Methods, Eq. 7) to understand the spin dynamics. During the quick collapse of P_x (see the top inset of Fig. 2B), the negative spin population ($P_z < 0$) reverses to positive ($P_z > 0$) in a short time ($\sim$2 s $\ll T_{1,0} \approx$ 21.5 s); this is the phenomenon of nuclear spin superradiance (*42*). In the stationary window, the spin population P_z remains negative (see the bottom inset of Fig. 2B). To extract the oscillation frequencies of the stationary maser, we quantitatively investigate its spectrum. We take a time trace from the stationary window after eliminating the initial transients and apply Fourier transform. Unlike the common maser spectrum (without periodic driving) that has a single peak at $\nu_0 \approx$ 8.915 Hz (Fig. 2C), four evident sidebands appear at $\nu_{\pm1} = \nu_0 \pm 0.900$ and $\nu_{\pm2} = \nu_0 \pm 1.800$ Hz (Fig. 2D), exactly at the frequencies of the transitions between Floquet states. All lines are at regular intervals equal to the periodic driving frequency ν_{ac}. In addition, the spectra of the Floquet maser for the case of $\nu_{ac} \geq \nu_0$ are presented in the Supplementary Materials (section S1). Our result confirms that a self-organized oscillation between Floquet states can build up. In addition, a 4000-s continuous oscillation gives a full width at half maximum (FWHM) of 0.3 mHz, which is two orders of magnitude narrower than the decoherence-limited resolution (≈30 mHz).

For a given Floquet system, the coupling to the periodic driving is characterized by the modulation index $\gamma B_{ac}/\nu_{ac}$. The Floquet maser discussed above was studied in the weak-coupling regime of $\gamma B_{ac}/\nu_{ac} \ll 1$. Strong-coupling regime ($\gamma B_{ac}/\nu_{ac} \gg 1$) is indispensable in various applications of nonlinear atomic spectroscopy (*32*) and strong-field physics (*43*). To reach this regime, previous work usually required a large B_{ac} and ν_{ac} larger than the decoherence-limited linewidth. However, a large magnetic field also affects the atomic magnetometer and deteriorates its performance (*44*).

We provide an alternative way to reach the strong-coupling regime by greatly decreasing the driving frequency ν_{ac} as low as submillihertz, much below the decoherence-limited resolution. Thus, the modulation index could be substantially larger than 1. For example, if a 0.050-Hz field with a magnitude of 56.15 nT drives ^{129}Xe, $\gamma B_{ac}/\nu_{ac} \approx$ 13.2. In Fig. 3A, the sideband spectrum based on the Floquet maser (red line) exhibits at least 25 evident comb-like symmetric lines centered at the Larmor-frequency line (at ν_0). Similarly, frequencies ν_{ac} lower than $T_{2,0}$-limited linewidth, e.g., ν_{ac}=10 mHz with amplitude 56.15 nT, correspond to modulation index $\gamma B_{ac}/\nu_{ac} \approx$ 66. In this case, we observe at least 134 maser sidebands (Fig. 3B), obtained from 4000-s continuous oscillation. Compared with the maser in the weak-coupling regime, a great number of Floquet transitions can build up stationary maser oscillations in the strong-coupling regime, enabling exact reconstruction of the Floquet energy levels.

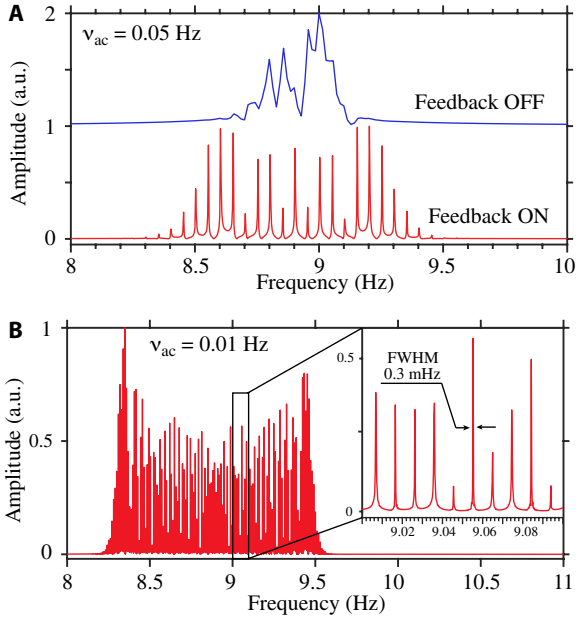

Fig. 3. Comb-like ultrahigh-resolution spectroscopy of Floquet maser. (**A**) Comparison between conventional Floquet spectrum based on ^{129}Xe free-decay signal (blue lines) and a spectrum based on Floquet maser (red lines). The driving frequency is ν_{ac} = 0.050 Hz, and its amplitude is B_{ac} = 56.15 nT. a.u., arbitrary units. (**B**) Spectrum based on Floquet maser, where ν_{ac} = 0.010 Hz and B_{ac} = 56.15 nT.

We emphasize the difference between our maser and existing masers. First, our maser is based on transitions between Floquet states, whereas existing masers usually exploit inherent transitions (*1*–*7*, *10*, *12*). Our maser generates sidebands that are easily tunable by changing the frequency and amplitude of the periodic driving. As shown in this work, the Floquet maser is well suited for sensing oscillating driving field with a frequency resolution, independent of the masing spin decoherence and limited only by the stability of the maser (see section S5). Second, unlike the conventional maser that uses a microwave cavity (*1*, *2*, *4*, *6*, *12*), our maser makes use of a feedback circuit based on the signal of an atomic magnetometer to provide damping feedback, enabling the maser frequency down to the audio-frequency range. Even though the oscillation frequency is much smaller than that of earlier established microwave masers (*1*, *2*, *4*, *6*, *12*), we show below that our demonstrated maser could be particularly useful for precision measurements, such as ultralow-frequency magnetic field sensing (*18*, *19*) and searching for ultralight new particles (*29*–*31*).

Applications of Floquet maser in magnetometry

Recently, experimental investigations have been reported toward achieving high sensitivity of measuring magnetic fields in low-frequency regime (1 to 100 mHz), which is of importance in applied (*19*) and fundamental physics (*18*, *29*–*31*). However, it remains challenging for state-of-the-art magnetometers to reach femtotesla-level sensitivity owing to substantial 1/*f* noise. Combining our demonstrated Floquet maser technique with magnetometry, we realize a sensitive magnetometer that is well suited for operation in the ultralow-frequency regime. As we show below, our maser-based magnetometer

can achieve subpicotesla-level sensitivity in the millihertz range. It would be possible to reach femtotesla-level sensitivity when the technical sources of maser instability are eliminated. The idea of our magnetometer is that the measured oscillating field applied to the spins can be seen as a periodic driving that generates sidebands around the maser oscillation frequency ($\nu_0 \gg 1$ Hz). Thus, the maser upconverts the low-frequency field to a higher frequency, where the $1/f$ noise arising from the Rb magnetometer is spectrally separated from the maser signal.

We first calibrate the magnetic response of the maser by applying an oscillating magnetic field with known amplitude and frequency. We focus on the prominent first-order sidebands occurring at $\pm\nu_{ac}$ about the central frequency, whose amplitude is proportional to $\mathcal{J}_1(\gamma B_{ac}/\nu_{ac}) \approx \gamma B_{ac}/2\nu_{ac}$ (here, we assume that the oscillating fields are small enough, satisfying $\gamma B_{ac}/\nu_{ac} \ll 1$). As shown in Fig. 4A, a 2.25-nT magnetic field is applied along the z direction, and its frequency ν_{ac} is swept from 1 to 22 Hz. We Fourier transform the individual measurement traces (with 60-s acquisition time) and record the corresponding sideband-peak amplitudes. The experimental amplitudes of first-order sidebands are fitted to a $1/\nu_{ac}$ function, which is in agreement with theory.

Similarly, we measure the amplitude response by applying a ν_{ac} = 1.000 Hz magnetic field with varying amplitude, as shown in Fig. 4B. The response of the maser to the applied oscillating field is measured to be $\xi_{maser}[\mathrm{V}] \approx 5.5 \times 10^{-3} B_{ac}[\mathrm{nT}]/\nu_{ac}[\mathrm{Hz}]$.

To show the noise performance of the maser-based magnetometer, we take a 4000-s maser real-time data without periodic driving and evaluate the corresponding power spectral density outside the spectral peak at ν_0. The background noise is different in different frequency ranges (see fig. S7): frequency dependent for frequencies below ~60 mHz and white (i.e., $\delta\xi_{maser} \approx 4 \times 10^{-5}$ V/Hz$^{1/2}$) for frequencies from ~60 mHz to 10 Hz. Combining with the above-calibrated response, the magnetic field sensitivity of maser-based magnetometer is shown in Fig. 4C. In the frequency above 60 mHz, the magnetic sensitivity is estimated to be $\delta B_{ac} \approx 7.2\nu_{ac}$ pT/Hz$^{1/2}$, where ν_{ac} is in hertz.

Below 60 mHz, the magnetic sensitivity reaches ~700 fT/Hz$^{1/2}$, which is mainly limited by the effective magnetic field fluctuations generated by ^{87}Rb magnetization (see sections S4 and S5). Such fluctuations arise from instability in both pump laser and vapor cell temperature, which can be overcome by using existing methods (*15*, *45*). By eliminating these sources of maser technical noise, it should be possible to reach a femtotesla-level sensitivity (see the red line in Fig. 4C). For example, after the elimination of technical noise, our maser-based magnetometer would achieve a sensitivity of about 7.2 fT/Hz$^{1/2}$ at 1 mHz, which is expected to be notably better than that in earlier work (*18*, *33*–*35*). The present device, therefore, is complementary to the state-of-the-art superconducting quantum interference devices (*33*) and atomic (*34*) magnetometers that have high sensitivity above 1 Hz. Our device is particularly sensitive between 1 mHz and 1 Hz. Moreover, our magnetometer can operate in a nonzero magnetic field (e.g., in Earth's field), in contrast with spin-exchange relaxation-free atomic magnetometers that operate at fields below ~100 nT (*44*).

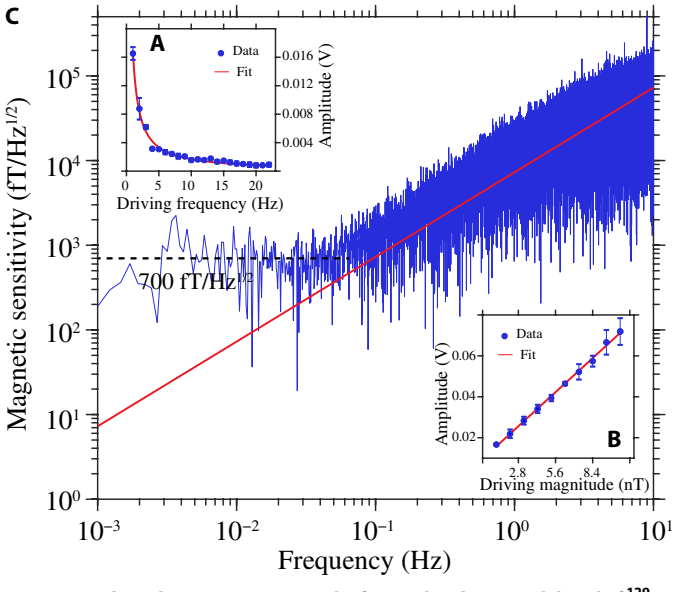

Fig. 4. Maser-based magnetometry on the first-order Floquet sideband of ^{129}Xe. (**A**) The first-order Floquet sideband amplitude follows a $1/\nu_{ac}$ dependence with the driving frequency ν_{ac}. The result of fit is $\xi = 0.017/\nu_{ac}$; B_{ac} = 2.25 nT. (**B**) The first-order Floquet sideband amplitude follows a linear dependence with the driving amplitude B_{ac}. The fit result is $\xi = 0.0055\, B_{ac} + 0.0096$, where ν_{ac} = 1.000 Hz. (**C**) Measured magnetic sensitivity of the maser-based magnetometer (note that the vertical and horizontal axes have a logarithmic scale).

DISCUSSION

We have reported a novel maser based on time-periodic Floquet systems. Unlike conventional masers, our maser oscillates at frequencies of transitions between Floquet states. The generalization of the notion maser to periodically driven systems opens a new avenue to explore Floquet physics unaffected by decoherence effects. As we show in this work, the connection of maser technique and Floquet physics allows observing ultrahigh-resolution spectra of Floquet systems with submillihertz widths and high-order sidebands effect. This can greatly improve the accuracy of measuring system energies, magnetic fields, atomic scalar and tensor polarizabilities (*28*), ultralight bosonic exotic fields (*31*), nonlinear multiphoton coherences (*32*), etc. Although demonstrated for ^{129}Xe spins, our scheme of Floquet maser can be transferred to other types of experimental systems. For example, recent advances in cold atoms (*23*, *24*) and dipolar spin ensembles (*25*) have led to progress in such areas of Floquet physics as time crystals and masers [for example, diamond maser (*4*, *12*)]. We suggest future theoretical and experimental studies of masers based on a variety of Floquet systems, taking a fresh look at many phenomena, such as Floquet Raman transitions (*25*), Mollow-triplet sidebands (*27*), Autler-Townes splitting (*46*), and even time crystals (*22*, *23*, *25*).

Our Floquet technique is generic and can be easily applied to well-established masers, such as hydrogen masers (*6*), diamond masers (*4*, *12*), and one-atom Rydberg maser (*47*), all promising as a new class of maser-based quantum sensors. For example, the application to hydrogen and diamond masers, whose gyromagnetic ratios are about three orders of magnitude larger than those of nuclei, yields improvements over currently achievable magnetic field sensitivity. As we show in this work, such sensors outperform state-of-the-art magnetometers (*18*, *33*–*35*) with subpicotesla sensitivity at millihertz frequencies and can be immediately applied, for example, in the searches of gravitational wave observatory eLISA (1 to 100 mHz) (*18*). Moreover, we show that couplings between masing spins (such

as protons or electrons) and oscillating exotic fields beyond the standard model (*20*) may enable their direct detection via Floquet maser magnetometry: The exotic fields are predicted to couple with standard model particles (masing spins in this case) and behave as an oscillating magnetic field, generating sidebands (*31*) on masing spins that can be measured with our maser. The maser can be applied to search for some exotic fields, such as ultralight axions (*29*–*31*) and other exotic spin-dependent interactions (*20*). Compared with existing approaches, our work has a unique advantage of measuring exotic fields with ultralow frequency, 1 to 100 mHz (corresponding to particle mass $\sim 10^{-18}$ to 10^{-15} eV). As discussed in Materials and Methods, our work is promising for improving the search sensitivity of axions by approximately two and three orders of magnitude compared to the values obtained in recent ultralow-field nuclear magnetic resonance experiments (*30*, *31*).

MATERIALS AND METHODS

Experimental apparatus

A cubic vapor cell containing 5-torr ^{129}Xe, 250-torr N_2 buffer gas, and a droplet of enriched ^{87}Rb is placed inside a five-layer cylindrical mu-metal shield and is resistively heated to 140°C. The longitudinal and transverse relaxation times of ^{129}Xe spins are measured to be $T_{1,0} \approx 21.5(2)$ s and $T_{2,0} \approx 13.65(1)$ s in a z bias field (≈750 nT). As shown in Fig. 1A, ^{129}Xe atoms are polarized by spin-exchange collisions with ^{87}Rb atoms (*36*), which are pumped with circularly polarized laser light (≈ 10 mW) propagating along $+z$. The pump laser frequency is tuned to the center of the buffer gas broadened and shifted D1 line. The ^{87}Rb atoms also act as a sensitive magnetometer for measuring the nuclear magnetization of the ^{129}Xe spins via optical rotation of linearly polarized probe laser light (≈1 mW) propagating along x. The frequency of the probe laser is detuned from the D2 transition by about 100 GHz. In the presence of a z-bias field, the ^{87}Rb magnetometer is primarily sensitive to the ^{129}Xe x-magnetization producing an effective magnetic field $B_{\text{eff}} = \frac{8\pi}{3}\kappa_0 M_x$ (*36*), where the enhancement factor κ_0 is about 500, and x-magnetization is $M_x = \mu_{\text{Xe}} n_{\text{Xe}} P_x$ with μ_{Xe}, n_{Xe}, and P_x being the ^{129}Xe nuclear magnetic moment, atomic density, and x-polarization, respectively. To suppress the influence of low-frequency noise, the polarization of the probe laser beam is modulated at 50 kHz with a photoelastic modulator, and the signal is demodulated with a lock-in amplifier.

The real-time output signal of the magnetometer generates the feedback field $B_f(t) = \chi P_x(t)$ on ^{129}Xe spins along y. The sign of feedback gain χ is simultaneously determined by the direction of the bias magnetic field ($+z$ or $-z$) and the connection polarity of the feedback coils ($+y$ or $-y$), i.e., $(+z, -y)$, $(-z, +y)$ for $\chi > 0$ and $(-z, -y)$, $(+z, +y)$ for $\chi < 0$. Here, we have considered that the atomic magnetometer is sensitive to the x magnetic field (or x-magnetization of ^{129}Xe) but with a negative sign; i.e., the magnetometer's output signal is proportional to "$-B_x B_z$" (*36*); thus, $(\pm z, \mp y)$ corresponds to $\chi > 0$ and similarly for the case of $\chi < 0$.

Energies and states of Floquet systems

A two-level spin system driven with a radio-frequency (rf) field can be treated as a dressed-spin system (*39*, *40*), in which rf photons with creation and annihilation operators $\hat{a}^\dagger$ and $\hat{a}$ are introduced by the second quantization of the rf field. Here, the rf field $B_{\text{ac}} \cos(2\pi\nu_{\text{ac}} t)$ is applied parallel to the static magnetic field $B_0\hat{z}$. The second-quantized Hamiltonian for the dressed-spin system can be written as (*40*).

$$\widehat{H}/2\pi = \nu_0 I_z + \nu_{\text{ac}} \hat{a}^\dagger \hat{a} + \lambda I_z (\hat{a}^\dagger + \hat{a}) \tag{1}$$

where $\nu_0 = |\gamma B_0|$ and $\gamma \approx -1.18 \times 10^7$ Hz/T is the gyromagnetic ratio of ^{129}Xe spins. The first term in Eq. 1 is the Zeeman interaction of the spin with B_0. The second term is the energy of the quantized rf field. The final term describes the coupling between the spin and the quantized rf field with strength $\lambda = \gamma B_{\text{ac}}/(2\sqrt{\bar{N}})$ (*40*), where $\bar{N} \gg 1$ is the average number of rf photons in the mode. We introduce basis states $|\pm, n\rangle$, where $|\pm, n\rangle = |\pm\rangle \otimes |n\rangle$, n signifies the rf photon number of the driving field, and $|\pm\rangle$ denotes the eigenstate of σ_z, i.e., $|+\rangle = (1,0)^{\text{T}}$ and $|-\rangle = (0,1)^{\text{T}}$. The Hamiltonian $\widehat{H}$ commutes with σ_z, and its diagonalization is reduced to that of $\hat{H}_\epsilon$ in each of the two subspaces of σ_z

$$\widehat{H}_\epsilon/2\pi = \frac{\epsilon}{2}\nu_0 + \nu_{\text{ac}} \hat{a}^\dagger \hat{a} + \frac{\epsilon}{2}\lambda(\hat{a}^\dagger + \hat{a}) \tag{2}$$

where $\epsilon = \pm 1$. A displacement operator is defined as $D(\xi) = e^{\xi\hat{a}^\dagger - \xi^* \hat{a}}$, which has the following properties: $D(\xi)D^\dagger(\xi) = 1$, $D(\xi)\hat{a}^\dagger D^\dagger(\xi) = \hat{a}^\dagger - \xi$, and $D(\xi)\hat{a}D^\dagger(\xi) = \hat{a} - \xi$. Then, $\widehat{H}_\epsilon$ in Eq. 2 can be written as follows

$$\widehat{H}_\epsilon/2\pi = D\left(-\frac{\epsilon\lambda}{2\nu_{\text{ac}}}\right)\left(\frac{\epsilon}{2}\nu_0 + \nu_{\text{ac}}\hat{a}^\dagger\hat{a} - \frac{\lambda^2}{4\nu_{\text{ac}}}\right)D^\dagger\left(-\frac{\epsilon\lambda}{2\nu_{\text{ac}}}\right) \tag{3}$$

This Hamiltonian $\widehat{H}_\epsilon$ has eigenstates $|\epsilon\rangle_n = D^\dagger\left(-\frac{\epsilon\lambda}{2\nu_{\text{ac}}}\right)|\epsilon, n\rangle$, i.e., the Floquet states. The energy of $|\epsilon\rangle_n$ is

$$E_{\epsilon,n}/2\pi = \epsilon\nu_0/2 + n\nu_{\text{ac}} \tag{4}$$

We now derive the explicit form of $|\epsilon\rangle_n$ for $n \approx \bar{N} \gg 1$ on the basis of $|\epsilon, n\rangle$. Let $\xi = -\frac{\epsilon\lambda}{2\nu_{\text{ac}}}$. By using the Glauber formula: $e^{A+B} = e^A e^B e^{[A,B]/2}$, where the two operators A and B both commute with their commutator, we have

$$\langle n - m| e^{\xi\hat{a}^\dagger - \xi^*\hat{a}} |n\rangle \approx e^{-\frac{\xi^*\xi}{2}} \mathcal{J}_{-m}(2\xi\sqrt{\bar{N}}) \tag{5}$$

As $|\xi| = \frac{\lambda}{2\nu_{\text{ac}}} = \frac{\gamma B_{\text{ac}}}{\nu_{\text{ac}}}\frac{1}{4\sqrt{\bar{N}}} \ll 1$, $e^{-\frac{\xi^*\xi}{2}} \approx 1$. Also, $2\xi\sqrt{\bar{N}} = -\frac{\epsilon\gamma B_{\text{ac}}}{2\nu_{\text{ac}}}$. Last, we obtain $\langle n - m| e^{\xi\hat{a}^\dagger - \xi^*\hat{a}} |n\rangle = \mathcal{J}_m\left(\frac{\epsilon\gamma B_{\text{ac}}}{2\nu_{\text{ac}}}\right)$, and the Floquet states are

$$\begin{aligned} |\epsilon\rangle_n &= |\epsilon\rangle \sum_m |n - m\rangle\langle n - m| e^{\xi\hat{a}^\dagger - \xi^*\hat{a}} |n\rangle \\ &= \sum_{n'} \mathcal{J}_{n-n'}\left(\frac{\epsilon\gamma B_{\text{ac}}}{2\nu_{\text{ac}}}\right)|\epsilon, n'\rangle \end{aligned} \tag{6}$$

As a result of the periodic driving, the two-level ($|+\rangle$, $|-\rangle$) spin system is extended to an infinite number of synthetic energy levels $|\epsilon\rangle_n$, as shown in Fig. 2A.

Maser mechanism with damping feedback

The feedback circuit uses a rubidium magnetometer to measure the nuclear polarization that acts back on the spins. The dynamics of the ^{129}Xe spin polarization $\vec{\mathbf{P}} = [P_x, P_y, P_z]$ is described by the nonlinear Bloch equations (*9*, *16*)

$$\begin{cases} \frac{dP_x}{dt} = P_y\omega_z(t) - P_z\omega_y(t) - \frac{1}{T_{2,0}}P_x \\ \frac{dP_y}{dt} = P_z\omega_x(t) - P_x\omega_z(t) - \frac{1}{T_{2,0}}P_y \\ \frac{dP_z}{dt} = P_x\omega_y(t) - P_y\omega_x(t) - \frac{1}{T_{1,0}}P_z + \gamma_{\text{se}}(P_{\text{Rb}} - P_z) \end{cases} \tag{7}$$

where $\vec{\omega} = 2\pi\gamma\vec{\mathbf{B}} = 2\pi\gamma\,[\,B_0 + B_{ac}\cos(2\pi\nu_{ac}t)\,]\hat{z} + 2\pi\gamma B_f(t)\,\hat{y}$. As the thermal polarization of ^{129}Xe is much smaller than that from spin-exchange collisions, we can neglect the thermal polarization in Eq. 7. The feedback field is $B_f(t) = \chi P_x(t)$, where χ is the feedback gain determined by the feedback circuit. The gain is $\chi = 0$ when the feedback circuit is disabled. P_{Rb} is the polarization of the rubidium atoms, which depends on the optical pumping and spin-relaxation rates (*36*). γ_{se} is the spin-exchange rate between the ^{129}Xe and ^{87}Rb. $\gamma_{se}(P_{Rb} - P_z)$ represents the spin-exchange pumping of ^{129}Xe spins. We now consider the spin dynamics in two cases.

1) We consider the condition: $P_z > 0$, $\chi < 0$ or $P_z < 0$, $\chi > 0$, corresponding to the experiments shown in Fig. 1 (B and D). In this case, maser phenomena cannot be generated. Here, we assume $B_{ac} = 0$. In the beginning, the ^{129}Xe spin polarization reaches an equilibrium state. After that, a magnetic field pulse along x tilts the spins away from the z to y axis by an angle θ_0, and the evolution of the spin polarization $\vec{\mathbf{P}}$ becomes (*9*, *16*)

$$\begin{aligned} P_+(t) &= P_0\,T_d\frac{q}{T_{2,0}}\mathrm{sech}\left[\frac{q}{T_{2,0}}(t-t_0)\right]e^{i(2\pi\nu t-\pi/2)} \\ P_z(t) &= P_0\,T_d/T_{2,0}\left\{q\tanh\left[\frac{q}{T_{2,0}}(t-t_0)\right]-1\right\} \end{aligned} \tag{8}$$

where $P_+ = P_x + iP_y$, ν is the oscillation frequency, and

$$\begin{aligned} q &= \left[1+(T_{2,0}/T_d)^2 + 2\cos\theta_0(T_{2,0}/T_d)\right]^{1/2} \\ t_0 &= -\frac{T_{2,0}}{q}\tanh^{-1}\left[\frac{1}{q}\left(\frac{T_{2,0}}{T_d}\cos\theta_0+1\right)\right] \end{aligned} \tag{9}$$

As demonstrated in the Supplementary Materials (section S2), the oscillation frequency has a small shift from the Larmor frequency ν_0, i.e., $\nu = \nu_0 + \Delta\nu$, arising from an effect known as frequency pulling (*16*). The shift $\Delta\nu$ linearly depends on the damping rate, i.e., $\Delta\nu = \alpha \cdot 1/T_d$, where $\alpha = 0.235$ in our experiments. Note that longitudinal relaxation is neglected here. $|P_+(t)|$ reaches its maximum value at $t = t_0$. We discuss two cases for the initial angle θ_0:

i) When the transverse excitation of nuclear spins is small ($|\theta_0| \ll 1$), $q \approx (1 + T_{2,0}/T_d)$ and $t_0 \to -\infty$. Because of $t_0 < 0$, $|P_\pm(t)|$ should be monotonically decreasing. Last, we have $P_+(t) \approx P_0 \sin\theta_0 e^{-(1/T_{2,0}+1/T_d)t}e^{i(2\pi\nu t-\pi/2)}$, which is a single-exponential decay (see Fig. 1B);

ii) When the initial angle is $\theta_0 \approx \pi$, $\cos\theta_0 \approx -1$ and $q \approx |\,1 - T_{2,0}/T_d\,|$. Although the form of Eq. 8 is complex, we can still gain information from Eq. 8. On the basis of the definition of t_0 as described above, when $T_d/T_{2,0} \geq 1$, we have $t_0 \leq 0$ and thus $|P_+(t)|$ should be monotonically decreasing; when $T_d/T_{2,0} < 1$, we have $t_0 > 0$ and $|P_+(t)|$ increases to be maximum at $t = t_0$ and then decreases to be zero (see Fig. 1D).

2) We consider the condition: $P_z > 0$, $\chi > 0$ or $P_z < 0$, $\chi < 0$ and $T_d/T_{2,0} < 1$, corresponding to the experiments shown in Fig. 2. In this case, the damping-induced torque provides a sufficient strength of feedback field for sustaining the maser oscillation. On the basis of numerical simulations, we show that the small transverse polarization component caused by misalignment or quantum fluctuation is sufficient for activating the Floquet maser (see section S3).

Estimation of search sensitivity for axion dark matter

Here, we discuss how to search for axions and axion-like particles (these are well-motivated dark matter candidates; we call these "axions" for brevity) via our maser technique and estimate the search sensitivity. As the nuclear spins of the maser on Earth move through the galactic dark matter halo, they couple to axion dark matter producing an effective oscillating magnetic field (*29*, *31*), generating axion-driven maser sidebands.

The effective magnetic field B_{axion}

$$\begin{cases} \nu_{axion} = m_{axion}c^2/h \\ B_{axion}\,[\mathrm{T}] \approx 6\cdot 10^{-8}\,g_{aNN}\,[\mathrm{Gev}^{-1}]/g_n \end{cases} \tag{10}$$

where m_{axion} is axion mass, c is the velocity of light, h is the Planck constant, $g_n \approx -3/2$ is the nuclear Landé g-factor for ^{129}Xe, and g_{aNN} is the coupling constant to be measured that represents the coupling strength of neutrons (from ^{129}Xe nucleus) and axions. For example, the axion mass of 10^{-18} to 10^{-15} eV corresponds to the frequency ν_{axion} of ~1 to 100 mHz. The experimental sensitivity (see Fig. 4C) of the maser-based magnetometer to real magnetic fields can directly translate to the sensitivity to the coupling constant g_{aNN}. As a result, we achieve the search sensitivity of axions $|\,g_{aNN}\,| \approx 1.75 \times 10^{-5}$ $\mathrm{Gev}^{-1}/\mathrm{Hz}^{1/2}$ for 1 to 60 mHz and $|\,g_{aNN}\,| \approx 1.8 \times 10^{-4}\nu_{axion}$ $\mathrm{Gev}^{-1}/\mathrm{Hz}^{1/2}$ from 60 mHz to 10 Hz. Benefitting from the narrow linewidth, the maser allows the detection of axion-driven frequency as low as millihertz (corresponding to axion mass ~10^{-18} eV). Current experiments, with measurement time $T_m = 10^4$ s and $\nu_{axion} = 1$ mHz, yield a potential of limit on $|\,g_{aNN}\,| \approx 1.75 \times 10^{-7}\mathrm{Gev}^{-1}$, well beyond the most stringent existing constraints (*30*, *31*).

SUPPLEMENTARY MATERIALS

Supplementary material for this article is available at http://advances.sciencemag.org/cgi/content/full/7/8/eabe0719/DC1

REFERENCES AND NOTES

1. J. P. Gordon, H. J. Zeiger, C. H. Townes, The maser—New type of microwave amplifier, frequency standard, and spectrometer. *Phys. Rev.* **99**, 1264–1274 (1955).
2. M. Oxborrow, J. D. Breeze, N. M. Alford, Room-temperature solid-state maser. *Nature* **488**, 353–356 (2012).
3. H. Kraus, V. A. Soltamov, D. Riedel, S. Väth, F. Fuchs, A. Sperlich, P. G. Baranov, V. Dyakonov, G. V. Astakhov, Room-temperature quantum microwave emitters based on spin defects in silicon carbide. *Nat. Phys.* **10**, 157–162 (2014).
4. J. D. Breeze, E. Salvadori, J. Sathian, N. M. Alford, C. W. M. Kay, Continuous-wave room-temperature diamond maser. *Nature* **555**, 493–496 (2018).
5. T. H. Maiman, Stimulated optical radiation in ruby. *Nature* **187**, 493–494 (1960).
6. H. M. Goldenberg, D. Kleppner, N. F. Ramsey, Atomic hydrogen maser. *Phys. Rev. Lett.* **5**, 361–362 (1960).
7. J. J. Cook, L. G. Cross, M. E. Bair, R. W. Terhune, A low-noise X-band radiometer using maser. *Proc. IRE* **49**, 768–778 (1961).
8. K. R. Chu, The electron cyclotron maser. *Rev. Mod. Phys.* **76**, 489–540 (2004).
9. M. Suefke, S. Lehmkuhl, A. Liebisch, B. Blümich, S. Appelt, Para-hydrogen raser delivers sub-millihertz resolution in nuclear magnetic resonance. *Nat. Phys.* **13**, 568–572 (2017).
10. H. Gilles, Y. Monfort, J. Hamel, ^{3}He maser for Earth magnetic field measurement. *Rev. Sci. Instrum.* **74**, 4515–4520 (2003).
11. P. Bevington, R. Gartman, W. Chalupczak, Magnetic induction tomography of structural defects with alkali–metal spin maser. *Appl. Optics* **59**, 2276–2282 (2020).
12. L. Jin, M. Pfender, N. Aslam, P. Neumann, S. Yang, J. Wrachtrup, R.-B. Liu, Proposal for a room-temperature diamond maser. *Nat. Commun.* **6**, 8251 (2015).
13. D. Bear, R. E. Stoner, R. L. Walsworth, V. A. Kostelecký, C. D. Lane, Limit on Lorentz and CPT violation of the neutron using a two-species noble-gas maser. *Phys. Rev. Lett.* **85**, 5038 (2000).
14. A. Derevianko, M. Pospelov, Hunting for topological dark matter with atomic clocks. *Nat. Phys.* **10**, 933–936 (2014).
15. T. E. Chupp, R. J. Hoare, R. L. Walsworth, B. Wu, Spin-exchange-pumped ^{3}He and ^{129}Xe Zeeman masers. *Phys. Rev. Lett.* **72**, 2363 (1994).
16. T. Sato, Y. Ichikawa, S. Kojima, C. Funayama, S. Tanaka, T. Inoue, A. Uchiyama, A. Gladkov, A. Takamine, Y. Sakamoto, Y. Ohtomo, C. Hirao, M. Chikamori, E. Hikota, T. Suzuki, M. Tsuchiya, T. Furukawa, A. Yoshimi, C. P. Bidinosti, T. Ino, H. Ueno, Y. Matsuo, T. Fukuyama, N. Yoshinaga, Y. Sakemi, K. Asahi, Development of co-located ^{129}Xe

and ^{131}Xe nuclear spin masers with external feedback scheme. *Phys. Lett. A* **382**, 588–594 (2018).
17. R. Moessner, S. L. Sondhi, Equilibration and order in quantum Floquet matter. *Nat. Phys.* **13**, 424–428 (2017).
18. I. Mateos, B. Patton, E. Zhivun, D. Budker, D. Wurm, J. Ramos-Castro, Noise characterization of an atomic magnetometer at sub-millihertz frequencies. *Sens. Actuat. A* **224**, 147–155 (2015).
19. J. Marfaing, J.-J. Bois, R. Blancon, E. Pozzo di Borgo, G. Waysand, S. Gaffet, M. Yedlin, P. Barroy, M. Auguste, D. Boyer, A. Cavaillou, About the world-wide magnetic-background noise in the millihertz frequency range. *Europhys. Lett.* **88**, 19002 (2009).
20. D. DeMille, J. M. Doyle, A. O. Sushkov, Probing the frontiers of particle physics with tabletop-scale experiments. *Science* **357**, 990–994 (2017).
21. M. S. Safronova, D. Budker, D. DeMille, D. F. J. Kimball, A. Derevianko, C. W. Clark, Search for new physics with atoms and molecules. *Rev. Mod. Phys.* **90**, 025008 (2018).
22. J. Zhang, P. W. Hess, A. Kyprianidis, P. Becker, A. Lee, J. Smith, G. Pagano, I.-D. Potirniche, A. C. Potter, A. Vishwanath, N. Y. Yao, C. Monroe, Observation of a discrete time crystal. *Nature* **543**, 217–220 (2017).
23. M. C. Rechtsman, J. M. Zeuner, Y. Plotnik, Y. Lumer, D. Podolsky, F. Dreisow, S. Nolte, M. Segev, A. Szameit, Photonic Floquet topological insulators. *Nature* **496**, 196–200 (2013).
24. A. Eckardt, Colloquium: Atomic quantum gases in periodically driven optical lattices. *Rev. Mod. Phys.* **89**, 011004 (2017).
25. Z. Shu, Y. Liu, Q. Cao, P. Yang, S. Zhang, M. B. Plenio, F. Jelezko, J. Cai, Observation of Floquet Raman transition in a driven solid-state spin system. *Phys. Rev. Lett.* **121**, 210501 (2018).
26. J. E. Lang, R. B. Liu, T. S. Monteiro, Dynamical-decoupling-based quantum sensing: Floquet spectroscopy. *Phys. Rev. X* **5**, 041016 (2015).
27. T. Joas, A. M. Waeber, G. Braunbeck, F. Reinhard, Quantum sensing of weak radio-frequency signals by pulsed Mollow absorption spectroscopy. *Nat. Commun.* **8**, 964 (2017).
28. Y. Zhang, M. Ciocca, L.-W. He, C. E. Burkhardt, J. J. Leventhal, Measurement of atomic polarizabilities using Floquet spectroscopy. *Phys. Rev. A* **50**, 1101–1106 (1994).
29. D. Budker, P. W. Graham, M. Ledbetter, S. Rajendran, A. O. Sushkov, Proposal for a cosmic axion spin precession experiment (CASPEr). *Phys. Rev. X* **4**, 021030 (2014).
30. T. Wu, J. W. Blanchard, G. P. Centers, N. L. Figueroa, A. Garcon, P. W. Graham, D. F. J. Kimball, S. Rajendran, Y. V. Stadnik, A. O. Sushkov, A. Wickenbrock, D. Budker, Search for axionlike dark matter with a liquid-state nuclear spin comagnetometer. *Phys. Rev. Lett.* **122**, 191302 (2019).
31. A. Garcon, J. W. Blanchard, G. P. Centers, N. L. Figueroa, P. W. Graham, D. F. J. Kimball, S. Rajendran, A. O. Sushkov, Y. V. Stadnik, A. Wickenbrock, T. Wu, D. Budker, Constraints on bosonic dark matter from ultralow-field nuclear magnetic resonance. *Sci. Adv.* **5**, eaax4539 (2019).
32. P. Glasenapp, N. A. Sinitsyn, L. Yang, D. G. Rickel, D. Roy, A. Greilich, M. Bayer, S. A. Crooker, Spin noise spectroscopy beyond thermal equilibrium and linear response. *Phys. Rev. Lett.* **113**, 156601 (2014).
33. Y. S. Greenberg, Application of superconducting quantum interference devices to nuclear magnetic resonance. *Rev. Mod. Phys.* **70**, 175–222 (1998).
34. D. Budker, M. Romalis, Optical magnetometry. *Nat. Phys.* **3**, 227–234 (2007).
35. J. M. Taylor, P. Cappellaro, L. Childress, L. Jiang, D. Budker, P. R. Hemmer, A. Yacoby, R. Walsworth, M. D. Lukin, High-sensitivity diamond magnetometer with nanoscale resolution. *Nat. Phys.* **4**, 810–816 (2008).
36. T. G. Walker, W. Happer, Spin-exchange optical pumping of noble-gas nuclei. *Rev. Mod. Phys.* **69**, 629–642 (1997).
37. A. Bienfait, J. J. Pla, Y. Kubo, X. Zhou, M. Stern, C. C. Lo, C. D. Weis, T. Schenkel, D. Vion, D. Esteve, J. J. L. Morton, P. Bertet, Controlling spin relaxation with a cavity. *Nature* **531**, 74–77 (2016).
38. N. Bloembergen, R. V. Pound, Radiation damping in magnetic resonance experiments. *Phys. Rev.* **95**, 8–12 (1954).
39. J. H. Shirley, Solution of the Schrödinger equation with a Hamiltonian periodic in time. *Phys. Rev.* **138**, B979 (1965).
40. C. Cohen-Tannoudji, J. Dupont-Roc, G. Grynberg, *Atom-Photon Interactions: Basic Processes and Applications* (John Wiley & Sons, 1992), chap. VI.
41. T. R. Gentile, P. J. Nacher, B. Saam, T. G. Walker, Optically polarized ^{3}He. *Rev. Mod. Phys.* **89**, 045004 (2017).
42. M. G. Benedict, *Super-radiance: Multiatomic Coherent Emission* (CRC Press, 2018).
43. G. D. Fuchs, V. V. Dobrovitski, D. M. Toyli, F. J. Heremans, D. D. Awschalom, Gigahertz dynamics of a strongly driven single quantum spin. *Science* **326**, 1520–1522 (2009).
44. I. K. Kominis, T. W. Kornack, J. C. Allred, M. V. Romalis, A subfemtotesla multichannel atomic magnetometer. *Nature* **422**, 596–599 (2003).
45. R. E. Stoner, M. A. Rosenberry, J. T. Wright, T. E. Chupp, E. R. Oteiza, R. L. Walsworth, Demonstration of a two species noble gas maser. *Phys. Rev. Lett.* **77**, 3971–3974 (1996).
46. C. N. Cohen-Tannoudji, The Autler-Townes effect revisited, in *Amazing Light*, R. Y. Chiao, Ed. (Springer, 1996), pp. 109–123.
47. D. Meschede, H. Walther, G. Müller, One-atom maser. *Phys. Rev. Lett.* **54**, 551 (1985).

Acknowledgments: We thank D. Suter, D. Sheng, W. H. Hai, M. Gu, Y. S. Zhang, J. M. Cai, A. Garcon, K. Asahi, T. E. Chupp, R. L. Walsworth, and J. W. Blanchard for valuable discussions. **Funding:** This work was supported by the National Key Research and Development Program of China (grant no. 2018YFA0306600), the National Natural Science Foundation of China (grant nos. 11661161018 and 11927811), and the Anhui Initiative in Quantum Information Technologies (grant no. AHY050000). M.J. acknowledges the support of the USTC Research Funds of the Double First-Class Initiative (grant no. YD3540002002). D.B. acknowledges the support of the European Research Council under the European Union's Horizon 2020 Research and Innovation Program under grant agreement no. 695405, the German Research Foundation (DFG) under the Reinhart Koselleck program, and the Cluster of Excellence Precision Physics, Fundamental Interactions, and Structure of Matter (PRISMA$^+$ EXC 2118/1) funded by the DFG within the German Excellence Strategy (project ID 39083149). **Author contributions:** M.J. designed and performed experiments, analyzed the data, and wrote the manuscript. H.S. and Z.W. performed the measurements and analyzed the data. X.P. proposed the experimental concept, devised the experimental protocols, and wrote the manuscript. D.B. contributed to the design of the experiment and proofread and edited the manuscript. All authors contributed with discussions and checking the manuscript. **Competing interests:** The authors declare that they have no competing interests. **Data and materials availability:** All data needed to evaluate the conclusions in the paper are present in the paper and/or the Supplementary Materials. Additional data related to this paper may be requested from the corresponding author.

Submitted 1 August 2020
Accepted 10 December 2020
Published 17 February 2021
10.1126/sciadv.abe0719

Citation: M. Jiang, H. Su, Z. Wu, X. Peng, D. Budker, Floquet maser. *Sci. Adv.* **7**, eabe0719 (2021).